Free-standing cross-linked hollow carbonaceous nanovesicle fibers with atomically dispersed CoN$_4$ electrocatalytic centers driving high-performance Li-S battery

Huifeng Zhuang [a], Tengfei Zhang [a], Hong Xiao [a], Fanchao Zhang [a], Pinyu Han [a], Hongfei Gu [c], Junrong Jiao [b,*], Wenxing Chen [c,*], Qiuming Gao [a,*]

[a] *Key Laboratory of Bio-inspired Smart Interfacial Science and Technology of Ministry of Education, Beijing Advanced Innovation Center for Biomedical Engineering, School of Chemistry, Beihang University, Beijing 100191, PR China*
[b] *Key Laboratory for Special Functional Materials of Ministry of Education, School of Materials Science and Engineering, Henan University, Kaifeng 475004, PR China*
[c] *Beijing Key Laboratory of Construction Tailorable Advanced Functional Materials and Green Applications, Experimental Center of Advanced Materials, School of Materials Science and Engineering, Beijing Institute of Technology, Beijing 100081, PR China*

ARTICLE INFO

ABSTRACT

Atomically distributed CoN$_4$ moieties within free-standing cross-linked hollow carbonaceous nanovesicle fibers (CoNCNF) are fabricated by electrostatic spinning following with thermal treatment. The conductive hollow carbonaceous nanovesicles are favorable for storage of electrolytes and fast transmission of electrons. The CoN$_4$ sites of CoNCNF film provide high-efficiency electrocatalytic sites for approving lithium polysulfides capture and fast kinetic transformation suppressing the shuttle effect. Using as cathode-separator interlayer, the CoNCNF-based Li-S battery presents a high initial capacity of 1023.9 mAh g^{-1} and an ideal capacity of 746.2 mAh g^{-1} maintains after 1000 cycles at 1 C. Interestingly, it easily performs 5000 cycles at a low decay rate of 0.016% at 2 C. Even at a high current density of 5 C, it provides an excellent capacity of 812.6 mAh g^{-1}. Surprisingly, it has a very high areal capacity of 10.7 mAh cm^{-2} when the cathode S mass loading is up to 12.5 mg cm^{-2}.

1. Introduction

Lithium-sulfur (Li-S) battery has attracted much more attention due to its high theoretical specific capacity (1675 mAh g^{-1}) and specific energy density (2600 Wh kg^{-1}) in the next-generation energy storage system [1–3]. In addition, many advantages such as nature abundant raw material of S, low cost and environmental benignity prove the feasibility of the battery system [4–7]. Despite these advantages, various challenges are still faced for the practical application of Li-S battery. In particular, the lithium polysulfides (LiPSs) intermediates Li$_2$S$_n$ (n = 4–8) are easily soluble in organic electrolytes and accumulate on the Li anode side through the separator for further reduction to form Li$_2$S [8]. This shuttle effect not only loses the cathode active material but also aggravates the corrosion and passivation of the Li anode, which eventually leads to a rapid capacity decay [9–11]. Therefore, suppressing the shuttle effect is the key to achieve high-performance Li-S battery, and it is extremely challenging [12,13].

Carbon-based materials were widely used to improve the electrochemical behavior due to their advantages in electrical conductivity, abundant morphology characteristics, corrosion resistance, light weight, etc. [14]. In particular, the carbonaceous non-woven fabrics film possessing of mutually cross-linked fibers may inhibit agglomeration and improve electrical conductivity observably superior to the powders [15–17]. The carbon fibers with suitable pore structure may effectively store electrolytes, facilitating ions transport by providing a small resistance and short diffusion pathway [18]. The unique free-standing film structure can be directly applied in the Li-S battery without further post-processing. Meanwhile, due to different chemical bonding properties of LiPSs (polar) and carbon (non-polar), the shuttle effect is difficult to effectively suppress because of their poor affinity and the low reaction kinetics towards LiPSs [19,20]. Therefore, suitable catalytic sites are also needed for efficient LiPSs capture and catalytic conversion to alleviate the shuttle effect [21–23]. Introduction of metal oxides, nitrides, sulfides and so forth with large polarity and catalytic ability could enhance the electrochemical performance of Li-S batteries because of the improved affinities and reaction kinetics towards LiPSs [24–26].

However, those compounds are usually limited by their own dense structures with high densities and low electroconductivities, which may lead to low loadings of sulfur and restrictedly catalytic abilities in the Li-S batteries. Metal single-atom catalysts (SACs) possessing of the advantages of unique geometric and electronic structures, high-activity electrocatalytic metal species, maximum atom utilization and so on, are of concern for energy conversion and storage [27–31]. Constructing the advanced metal SACs with optimized morphology, pore structure and texture, catalytic centers, etc. to achieve efficient immobilization and fast kinetic transformation of LiPSs, is a great challenge for the high-performance Li-S batteries.

Herein, we successfully implant atomically distributed CoN_4 moieties in one-dimensional (1D) free-standing cross-linked hollow carbon nanovesicle CoNCNF fibers film and apply it as the cathode-separator interlayer for Li-S battery. The unique polar CoN_4 sites provided valid reactive sites for efficient LiPSs capture and fast kinetic transformation. The hollow carbon nanovesicles are favorable for storage of electrolytes facilitating ions transport and their prominent conductive walls of the well contacted holes are more conducive to the fast transmission of electrons. A high initial capacity of 1023.9 mAh g^{-1} was obtained for the assembled Li-S battery based on implanted CoNCNF interlayer and the capacity of 746.2 mAh g^{-1} was gotten after 1000 cycles at 1 C. After 5000 cycles, a very low decay rate of 0.016% was achieved at 2 C. A high capacity of 812.6 mAh g^{-1} was achieved at the high current density of 5 C. When the cathode S mass loading was up to 12.5 mg cm^{-2}, a high areal capacity of 10.7 mAh cm^{-2} was harvested for the Li-S battery.

2. Experimental section/methods

2.1. Synthesis of ZIF-8

4.76 g of $Zn(NO_3)_2 \cdot 6H_2O$ was dissolved in a mixture of 72 mL of dimethylformamide (DMF), 24 mL of ethanol and 24 mL of methanol and stirred for 2 h to obtain solution **A**. 5.254 g of dimethylimidazole was dissolved in a mixture of 24 mL of DMF and 16 mL of methanol and stirred for 2 h to obtain solution **B**. The above solutions **A** and **B** were mixed and then stirred for 6 h and left for 18 h. The precipitate was collected by centrifugation and washed 3 times with methanol, dried at 80 °C for 24 h to obtain ZIF-8.

2.2. Syntheses of CoNCNF, NCNF and CoNC

CoNCNF was synthesized using an electrospinning process. Firstly, 0.5 g of ZIF-8, 0.5 g of polyacrylonitrile (PAN, $M_w = 130,000$) and 17 mg of $Co(NO_3)_2 \cdot 6H_2O$ were dissolved in 5 g of DMF and stirred well to obtain a homogeneous solution. The precursor solution was transferred to a syringe with a stainless steel needle. The spinning solution was pushed at a rate of about 1 mL h^{-1} with an operating voltage of 18 kV. The spun filaments were collected using a roller device at a distance of 18 cm and a speed of 200 r min^{-1}. The primary nanofibers obtained were pre-oxidized in air at 220 °C for 2 h and then carbonized in a nitrogen gas stream at 900 °C for 2 h with a ramp rate of 5 °C min^{-1}. Finally, the calcined material was thoroughly washed in H_2SO_4 solution (4.0 M) for 12 h with the aim of removing the residual Zn species. CoNCNF was obtained after thorough washing with distilled water with ethanol and drying. For comparison, the product NCNF was obtained using the same preparation process without the addition of Co $(NO_3)_2 \cdot 6H_2O$ in the preparation of the spinning solution. CoNCNF was ball-milled for 6 h to obtain CoNC powder after disruption of the fiber structure. The CoNC powder is mixed with PVDF in the ratio of 9: 1 by mass and then dispersed in a certain amount of DMF to form a homogeneous solution. After vacuum filtration, the CoNC powder is uniformly covered on the surface of Celgard 2400 separator, dried sufficiently and cut into a circle of 19 mm diameter. The surface weights of CoNCNF, NCNF and CoNC powder are 1–1.5 mg cm^{-2}.

2.3. Synthesis of the sulfur cathode

The sulfur powder, acetylene black, carbon nanotubes and PVDF in the mass ratio of 6: 2: 1: 1 were stirred thoroughly in an appropriate amount of N-methylpyrrolidone (NMP) to obtain a slurry and then uniformly coated on the aluminum foil and dried under vacuum at 60 °C for 12 h. After cutting, cathode sheets with a sulfur surface loading of about 1.44 mg cm^{-2} were obtained. The cathode sheets with high surface loading of 12.5 mg cm^{-2} could be produced by increasing the coating thickness, respectively.

2.4. Material characterization

X-ray diffraction (XRD) patterns of the samples were recorded on an X-ray diffractometer (XRD-6000) with Cu K_α ($\lambda = 0.15418$ nm) with a scanning range of 10–80° at a speed of 6° min^{-1}. Raman spectra were collected on a (HR-800). The morphologies and structures were surveyed by high resolution transmission electron microscopy (HRTEM, JEOL 2100 F) and a scanning electron microscope (SEM, JSM-7500 F). Aberration-corrected high-angle annular dark-field scanning transmission electron microscopy (HAADF-STEM) image and energy dispersive X-ray spectroscopy elemental mapping (EDS) were obtained on JEOL JEM-ARM300F. X-ray photoelectron spectroscopy (XPS) measurements were carried out on Thermo Scientific ESCALAB 250. X-ray absorption fine structure spectra (XAFS) were collected at the 1W1B station in Beijing Synchrotron Radiation Facility (BSRF). The amount of cobalt in CoNCNF was measured by inductively coupled plasma optical emission spectrometer (ICP-OES, iCAP 7400, Thermo, Waltham, USA). XPS patterns of the samples were recorded on K-alpha 1063 equipment (Al K_α ray source).

2.5. Calculational details

The density functional theory (DFT) calculations were performed in materials studio. The OTFG ultrasoft pseudopotentials and Perdew-Burke-Ernzerhof (PBE) Generalized gradient approximation (GGA) were adopted. The energy cutoff was set to 520 eV. The structures were relaxed until the forces acting over all atoms were less than 0.05 eV $Å^{-1}$, and electronic energies were converged in the range of 2×10^{-5} eV. To remove the interaction between successive slabs, a vacuum distance larger than 20 Å was used.

The adsorption energy (E) of Li was defined as:

$$E = E_{total} - E_{sur} - E_{Li_2S_n}$$

where the E_{total}, E_{sur} and $E_{Li_2S_n}$ are the energy of surface bound with a Li_2S_n ($1 \leq n \leq 8$) molecules, the pristine surface and Li_2S_n ($1 \leq n \leq 8$) molecules, respectively. The Gibbs free energy (ΔG) of the reactions of CoNCNF with various soluble Li_2S_n was investigated and calculated by the following formula:

$$\Delta G = G_{total} - G_{sur} - G_{Li_2S_n}$$

where the G_{total}, G_{sur} and $G_{Li_2S_n}$ are the free energy of surface bound with a Li_2S_n ($1 \leq n \leq 8$) molecules, the pristine surface and Li_2S_n ($1 \leq n \leq 8$) molecules, respectively. The free energy was calculated by the following formula:

$$G = E - ZPE + \int CpdT - TS$$

where the E, ZPE, S, T are the binding energy, zero point energy change, entropy change of adsorption reaction and temperature of reaction, respectively.

2.6. Symmetrical cell assembly and catalytic effect test

The CoNCNF was cut into discs with an area of 1 cm^{-2} and used directly as electrodes. The electrodes were assembled into CR2025 coin cells on both sides using a polysulfide solution (0.25 M Li$_2$S$_6$ and 1 M lithium bis(trifluoroethanesulfonate)imide (LiTFSI) in 1,2-dimethoxyethane (DME) and 1,3-dioxolan (DOL) in a volume ratio of 1: 1) as the electrolyte. The assembled symmetric cells were scanned at −1.0 and 1.0 V with a scan rate of 10 mV s^{-1}.

2.7. Li$_2$S nucleation measurement

The obtained CoNCNF electrode was used as the cathode with lithium foil as the anode to assemble a CR2025 coin cell. 0.25 M Li$_2$S$_6$ and 1 M LiTFSI in DME/DOL (v/v = 1: 1) were used as the cathode electrolyte, and the anode electrolyte was used as the original electrolyte without the addition of Li$_2$S$_6$. The cells were discharged at a constant current density of 0.112 mA to 2.09 V, and then kept at a constant potential of 2.05 V for Li$_2$S nucleation and growth until the current dropped to 10^{-5} A.

2.8. Cell assembly and electrochemical test

CR2025 coin cell is assembled with sulfur electrode as cathode, freestanding CoNCNF/ NCNF wafer placed between cathode and separator, lithium foil as anode and Celgard 2400 as separator. The electrolyte was 1 M LiTFSI in DME/DOL (v/v = 1: 1) with 2% LiNO$_3$ as additive. All CR2025-type coin cells were assembled in a glove box filled with argon (O$_2$ < 0.1 ppm, H$_2$O < 0.1 ppm). Galvanostatic cycling was conducted using a LAND 8-channel battery tester (LAND CT2001A), and the charge-discharge voltage range is 1.7–2.8 V. The cyclic voltammetry (CV) test was recorded between 1.7 and 2.8 V on CHI660D electrochemical workstation, and the frequency range of Electrochemical impedance spectroscopy (EIS) measurement was set between 100 kHz and 0.01 Hz.

2.9. Li$_2$S$_6$ adsorption test

30 mg of sample was added to 3 mL of Li$_2$S$_6$ solution (5 mM, solvent DOL/DME, v/v = 1: 1). After standing for 12 h, the photos of the adsorption result were taken with a digital camera. The supernatant was tested by Tsushima, Japan UV-3600 spectrometer.

3. Results and discussion

3.1. Fabrication and physicochemical characteristics of the CoNCNF film

The preparation of CoNCNF films mainly includes electrostatic spinning and subsequent thermal treatment with the schematic diagram shown in Fig. 1a. Briefly, a homogeneous mixture consisting of ZIF-8 dodecahedral nanocrystals (size: ~200 nm, Fig. S1), Co(NO$_3$)$_2$·6H$_2$O and polyacrylonitrile (PAN) was firstly electrostatically spun into primary fibers. During the subsequent high-temperature thermal treatment, the internal components of ZIF-8 were decomposed and diffused
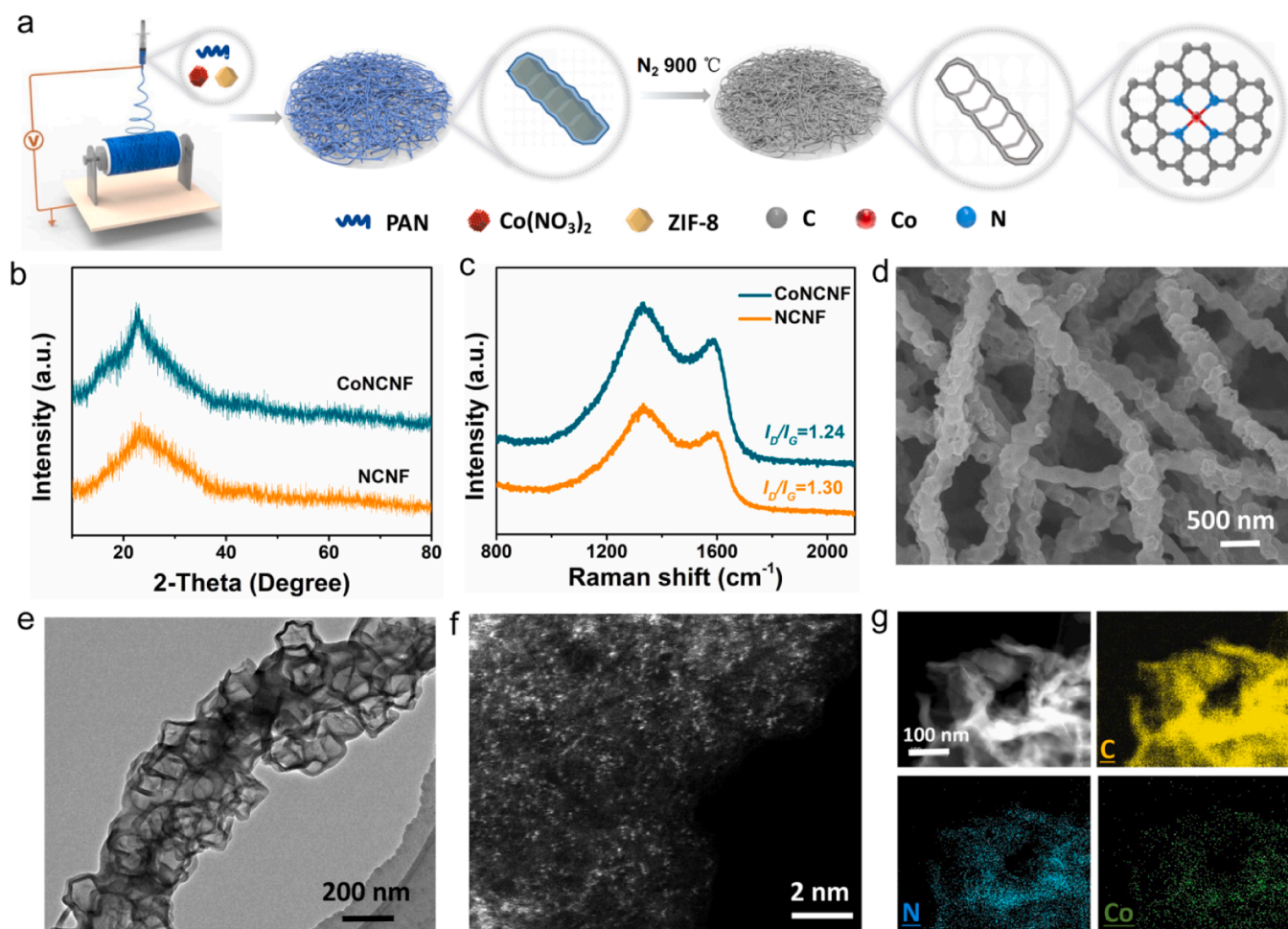
Fig. 1. (a) Schematic synthesis of CoNCNF. (b) XRD and (c) Raman spectra of CoNCNF and NCNF. (d) SEM, (e) HRTEM and (f) magnified HAADF-STEM images of CoNCNF. And (g) EDS mapping of CoNCNF.

into the PAN fibers and subsequently carbonized, forming nanovesicles in their original positions. Only one broad diffraction peaks at about 24.8° indexed to the (002) planes of graphitized carbon was found in the XRD patterns (Fig. 1b) of CoNCNF without retrieving diffraction peaks of metallic Co and its oxides, which is highly consistent with the single-atom Co character. Since the (002) planes of pure carbon is at about 26°, the small shift toward low angle for the XRD peak is due to the formation of Co-N bond with a longer bond length than C-C in the carbonaceous framework. Raman spectra (Fig. 1c) showed a lower I_D/I_G ratio proving the more completed graphitization of the sp^2 hybridization of carbon in CoNCNF which may result in a more superior electrical conductivity of the substrate. The typically prepared CoNCNF non-woven fabrics have the thickness of about 100 μm (Fig. S2) where the film is composed of nanofibers with the diameter of about 400 nm (Fig. 1d), similar to those of NCNF without single-atom Co (Fig. S3). TEM image (Fig. 1e) of the CoNCNF presents a unique polyhedra in shape hollow nanovesicles with the sizes of about 50 nm. Clearly, the hollow structure inherited the morphology of ZIF-8 dodecahedral nanocrystals and the shrunk sizes could be due to the thermal treatment. The hollow carbon nanovesicles may be favorable for storage of electrolytes facilitating Li$^+$ transports in the Li-S battery. The hollow carbon nanovesicles are closely contacted and aggregated into a 1D structure of fibers and they cross-linked with each other maintaining a certain free-standing structure. The very low Brunauer-Emmett-Teller (BET) surface area (Fig. S4a, NCNF: 25.6 m^2 g^{-1}, CoNCNF: 41.3 m^2 g^{-1}) indicates that the carbonized samples form dense carbon walls for the well contacted holes which could be conducive to the fast transmission of electrons. The electrolytes can penetrate into the interior of the vesicles through the pores with a diameter of about 1.5 nm based on the pore size distribution analysis (Fig. S4b). No obvious Co related particle aggregation was found from the TEM image (Fig. 1e) indicating the atomically distributed Co, which is consistent with the XRD analysis. HAADF-STEM can directly distinguish the Co elements from the adjacent light elements. As shown in Fig. 1f, the large number of white dots distributed on the black background of CoNCNF are considered as multiple isolated Co atoms due to the different light and dark lining of Co, N and C elements. The uniform distribution of C, N and Co elements was demonstrated by EDS (Fig. 1g), and no significant Co accumulation was found. The cobalt content of 1.13 wt% was obtained by ICP-OES measurement. The prepared CoNCNF film can be cut into arbitrary shapes and maintain excellent flexibility (Fig. S5).
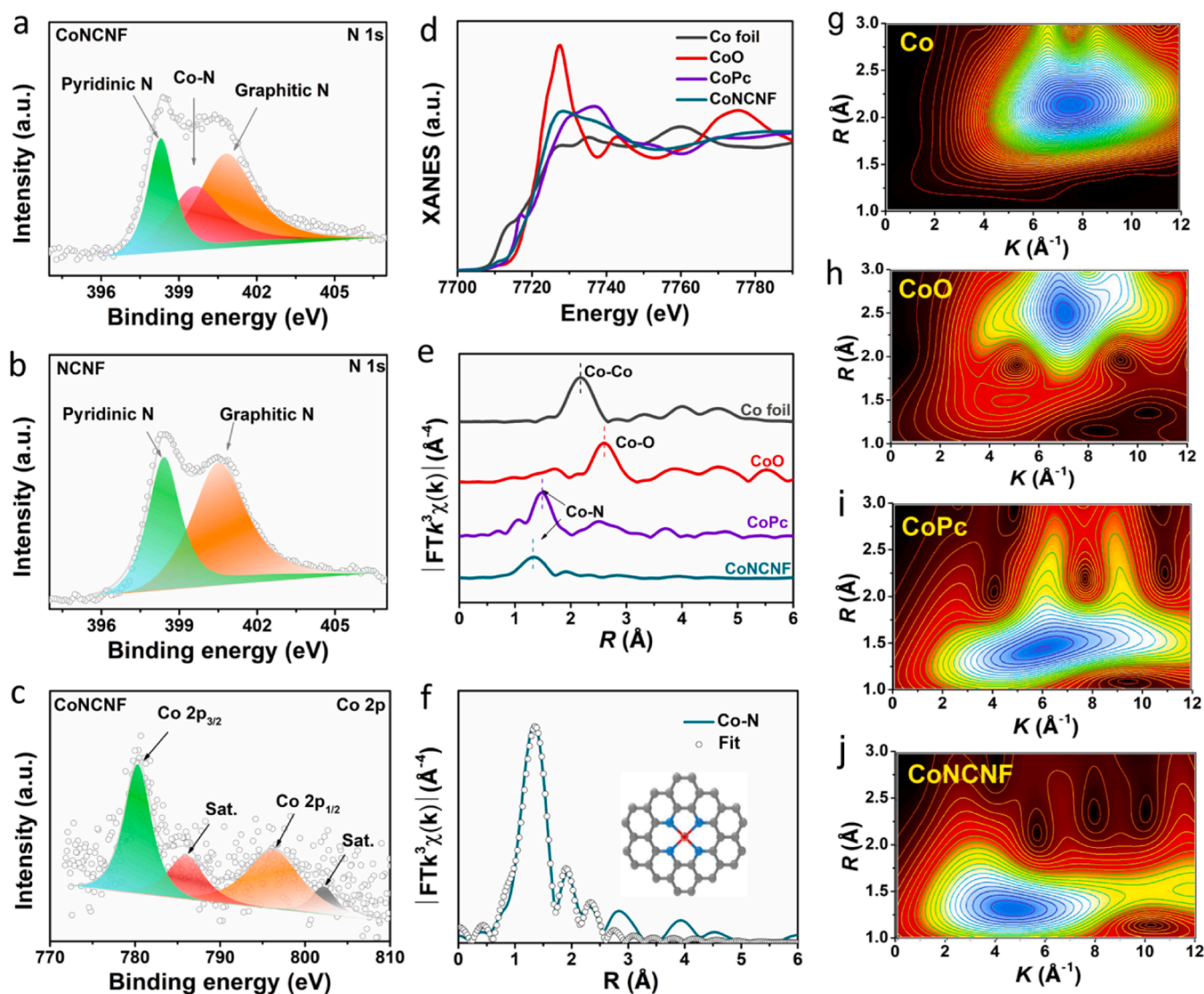

Fig. 2. N 1s XPS spectra of CoNCNF (a) and NCNF (b). (c) Co 2p XPS spectra of CoNCNF. (d) The experimental Co K-edge XANES spectra of CoNCNF and the references (Co foil, CoO and CoPc). (e) FT k^3-weighted Co K-edge EXAFS spectra of CoNCNF and the references. (f) FT-EXAFS fitting curves of CoNCNF at Co K-edge, inset is the Co-N$_4$ structure. And WT-EXAFS plots of Co foil (g), CoO (h), CoPc (i) and CoNCNF (j), respectively.

3.2. Microstructure analyses for the CoNCNF material

High-resolution N 1s XPS spectra of both CoNCNF (Fig. 2a) and NCNF (Fig. 2b) show two typical deconvoluted peaks of pyridinic N (398.3 eV) and graphitic N (400.9 eV) [32]. Differently, the deconvoluted peak at 399.7 eV unique to CoNCNF is well attributed to the Co-N bond [33]. The contents of pyridinic N and Co-N bonds in CoNCNF increased with implantation of cobalt based on the analysis of the peak areas. The high contents of pyridinic N and Co-N bonds can effectively increase the electron-donating capacity of the catalyst host, thus facilitating the increase of redox kinetics to improve the catalytic activity [34]. In addition, the Co 2p peaks (Fig. 2c) centered at 796.2 and 780.3 eV and the associated satellite peaks (802.2 and 785.9 eV) can be well attributed to the $2p_{1/2}$ and $2p_{3/2}$ of the Co-N bond in the evaluation of the Co 2p spectral peaks [33]. These results suggest that the atomically dispersed Co has a typical Co-N coordination environment. The microstructure of CoNCNF at the atomic scale was studied by using XAFS. The position of the Co K-edge absorption threshold reflects the average oxidation state of the Co species. As shown in Fig. 2d, the edge position of the CoNCNF is between Co foil and CoO, which implies that the valence state of the Co element is between 0 and + 2 [35]. The extended Fourier transform (FT) extended X-ray absorption fine

structure (EXAFS) spectra of CoNCNF is shown in Fig. 2e, highlighting a dominant peak located at 1.4 Å, which is mainly attributed to the scattering of the Co-N coordination [36]. No significant Co-Co peak was detected near 2.2 Å, proving that Co atoms did not aggregate to form metal particles [37]. Due to the strong resolution in both *k* and *R* spaces, the atomic configuration of the CoNCNF was investigated by applying the Co K-edge wavelet transform (WT)-EXAFS. The WT curve (Fig. 2g-j) of the CoNCNF shows a WT maximum at 6 $Å^{-1}$ attributed to the Co-N bond compared to the Co foil and CoO [27]. The structural parameters of the Co K-edge were extracted by least square EXAFS fitting. The results are shown in Fig. 2f, S6 and Table S1. It can be concluded that the coordination number of the central atom Co is four, which is directly connected by one Co atom and four N atoms, and the average bond length is 1.99 Å [38].

3.3. Electrocatalytic properties of the CoNCNF

The adsorption ability of materials on LiPSs plays an important role in the electrocatalytic effect. Therefore, we calculated the adsorption energy of both CoNCNF and NCNF materials for S_8, Li_2S_8, Li_2S_6, Li_2S_4, Li_2S_2 and Li_2S, respectively, and recorded them in Fig. 3a with the adsorption configurations shown in Fig. 3b. It is obvious that CoNCNF
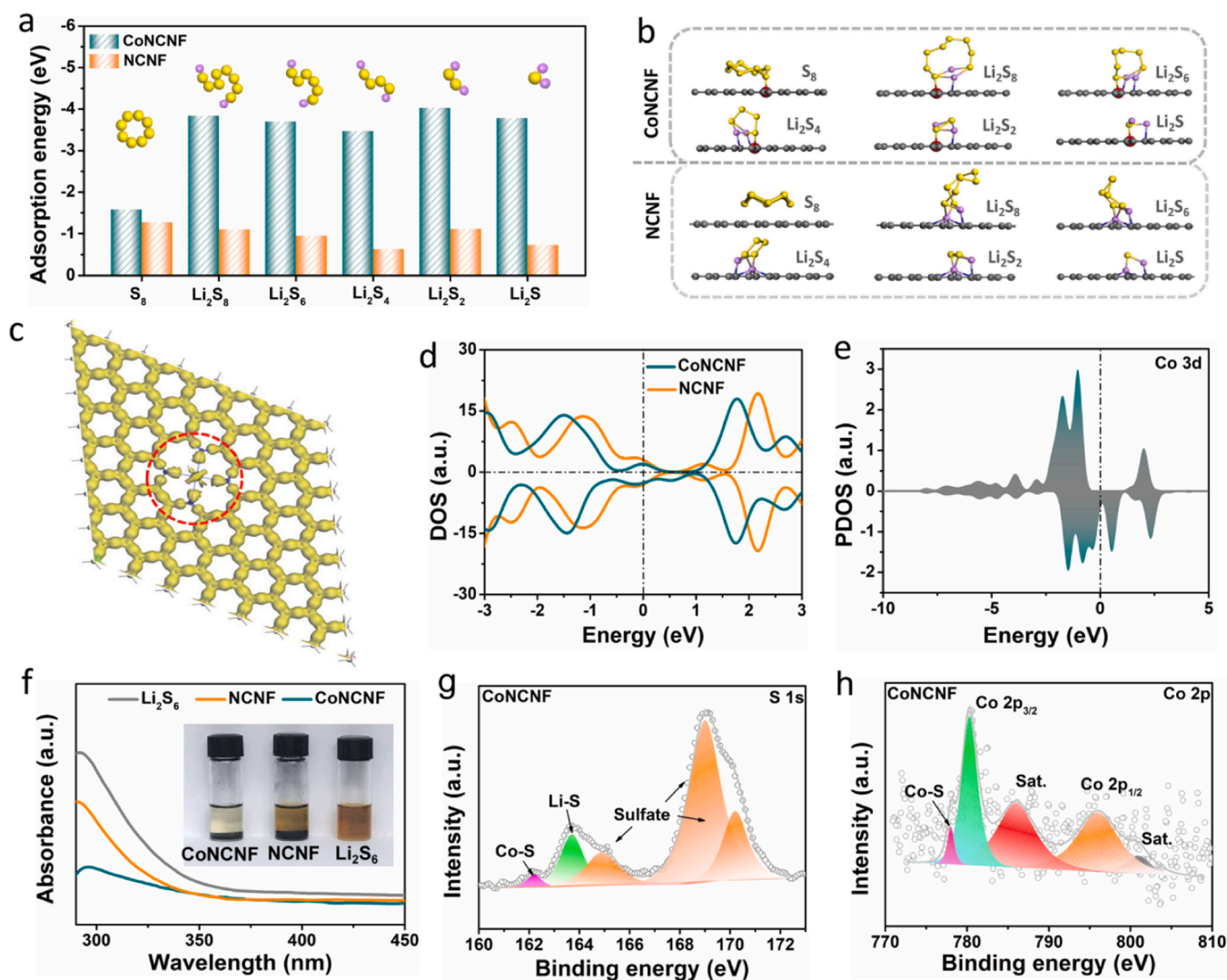

Fig. 3. (a) The adsorption energy of CoNCNF and NCNF for polysulfides and (b) the corresponding adsorption configuration calculated by DFT. (c) Electron density difference image of CoNCNF. (d) Density of states of CoNCNF and NCNF. (e) Partial density of state for the Co 3d orbital of CoNCNF. (f) UV–Vis absorbance spectra and optical images (inset) of Li_2S_6 solution after interaction with different catalysts. And XPS spectra of S 1 s (g) and Co 2p (h) after adsorption of CoNCNF.

has a stronger adsorption capacity for LiPSs. The electron density difference image (Fig. 3c) indicates that the electrons in CoNCNF are more favorable for transmission near the Co atoms. Density of states calculations were performed on the samples in order to probe more deeply into the adsorption and catalytic mechanism. The results show that introduction of single-atom Co in CoNCNF leads to the formation of new hybridization energy bands near the Fermi energy level (Fig. 3d), which would make it easier for electrons to jump. From partial density of states it could be concluded that the hybridization energy bands are mainly caused by the 3d orbitals of Co (Fig. 3e). The easier electrons leap facilitates the electrons exchange between catalyst and polysulfides, which effectively promotes the adsorption and catalytic processes. Fig. 3f (inset) shows more visually that CoNCNF has better adsorption properties. UV–vis absorption spectra also confirm that the Li_2S_6 solution has the lowest solute (Li_2S_6) content in the supernatant after adsorption of CoNCNF. XPS (Fig. 3g, h) of the adsorbed CoNCNF sample clearly presents the generation of unique Co-S bonds, which further confirms the strong adsorption of Co with S.

To demonstrate the electrocatalytic activity, a symmetric cell was assembled using a free-standing CoNCNF film as electrode and 0.25 M Li_2S_6 solution as electrolyte and evaluated by CV. The test results are shown in Fig. 4a, where typical reversible redox peaks were retrieved. During discharge process the active reactant (Li_2S_6) was first reduced to short-chain LiPSs and finally to Li_2S [39]. Li_2S was reversibly oxidized to LiPSs and eventually elemental S during the reverse charge process [39].

The CoNCNF exhibits a higher current response and the Tafel plot (Fig. 4b) further shows that the exchange current of the CoNCNF (3.17 mA cm^{-2}) symmetric cell is much higher than that of the NCNF (0.75 mA cm^{-2}), indicating faster charge transfer. Meanwhile, CV test of the CoNC symmetric cell shows a very weak peak current response (Fig. S7). Conducting the bulk resistance test for CoNCNF, NCNF and CoNC, we found that the CoNC sample with the disrupted 1D structure has the largest bulk resistance while CoNCNF has the smallest (Fig. S8). Therefore, we deduce that the high catalytic activity of CoNCNF is attributed to the implantation of single-atom Co causing the electron jump, and the cross-linked carbon fiber host composed of dense carbon wall is more favorable for electrons transmission to enhance the catalytic rate. In addition, the Nyquist plots (Fig. S9) of the symmetric cell show that the CoNCNF has a smaller interfacial and charge transfer impedance, which is more favorable for the electrocatalysis. To evaluate the catalytic function of CoNCNF for conversion of liquid Li_2S_6 to solid Li_2S, potentiostatic nucleation experiments were used to verify the electrochemical deposition process of Li_2S. The results are recorded in Fig. 4c, and it is clear that CoNCNF describes a much earlier and higher discharge current peak (2543 s, 0.430 mA) than that of NCNF (4126 s, 0.251 mA). In addition, the Li_2S electrodeposition capacity of the CoNCNF cathode was 482.1 mAh g^{-1}, which is significantly higher than that of the NCNF cathode at 288.8 mAh g^{-1}. The results indicate that the implantation of single-atom Co effectively improves the kinetics of Li_2S_6 to Li_2S transition and enhances the nucleation capacity of Li_2S. Fig. 4d
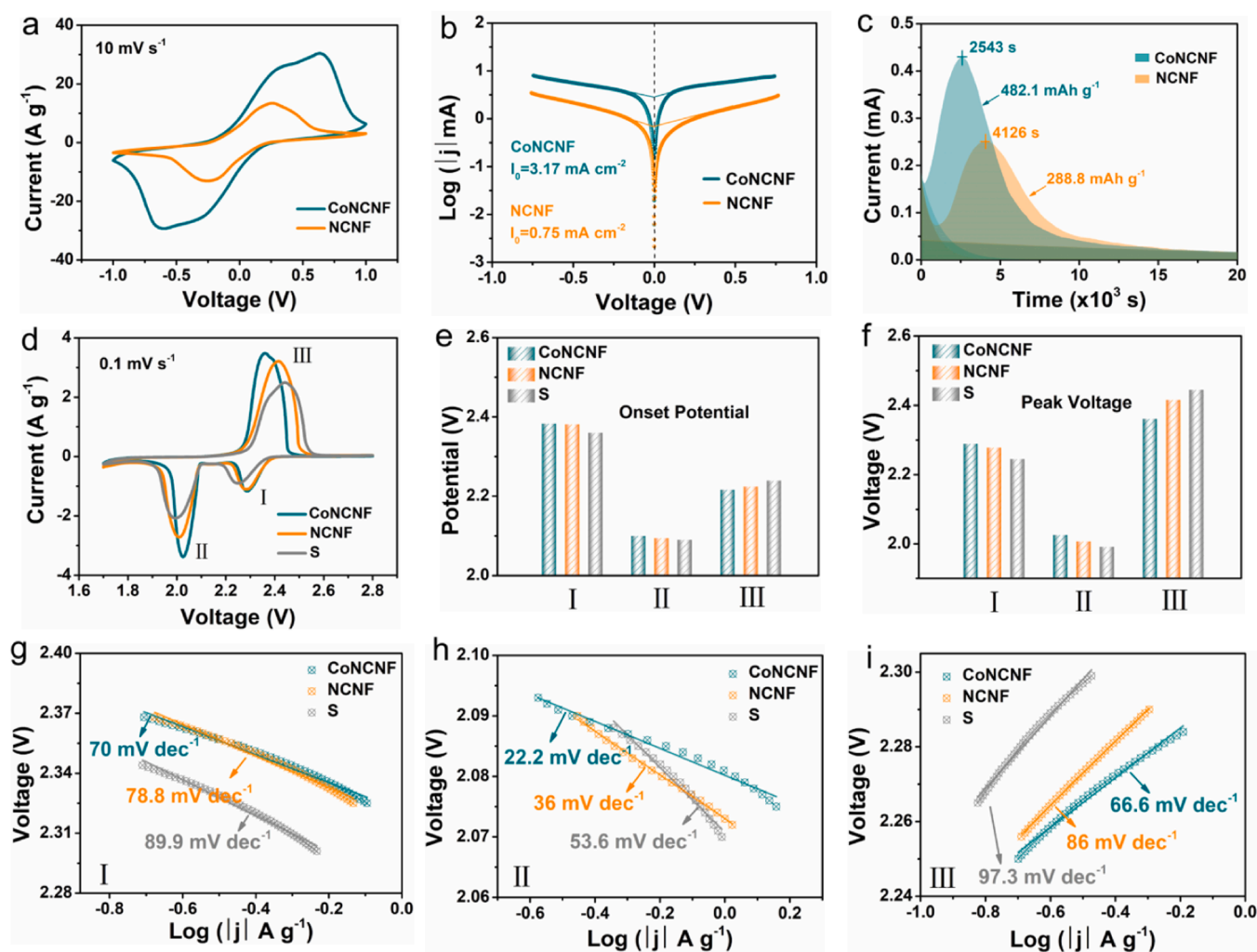

Fig. 4. (a) CV, (b) Tafel plot and (c) potentiostatic discharge curves of the symmetrical cells with the CoNCNF and NCNF electrodes in the electrolytes with Li_2S_6. (d) CV curves and (e) the corresponding peak voltage, (f) onset potential and (g-i) Tafel plot of cells based on CoNCNF, NCNF and bare S samples.

shows the CV curves of the Li-S cell for different samples at 0.1 mV s^{-1}. Each sample was clearly retrieved with a typical redox peak, which is associated with a reversible redox reaction of sulfur species. It is noteworthy that the highest peak intensities are found for the cells corresponding to CoNCNF, followed by NCNF and the last for bare S. Higher peak intensities indicate stronger kinetics of the corresponding redox reactions. For a more convenient visualization of the CV peaks, the data of the onset potential and peak voltage of each peak were organized and are recorded in Fig. 4e-f. The onset potential and peak voltage of the reduction peaks (I, II) of CoNCNF correspond to larger potentials and voltages than those of the other samples, indicating that the reduction reaction is more favorable. In other words, the earlier appearance of the current response confirms that the energy barrier required for the reduction of sulfur species is lower. Similarly, the peak (III) position of CoNCNF in the reverse oxidation process shows that it has an optimal catalytic function for the conversion of Li$_2$S to S. In addition, the catalytic activity of CoNCNF was further quantitatively analyzed by the Tafel plots (Fig. 4g-i). The CoNCNF displayed the small Tafel slopes of 70 (peak I), 22.2 (peak II) and 66.6 mV dec^{-1} (peak III) in the three redox peaks compared to those of NCNF (78.8, 36 and 86 mV dec^{-1}) and bare S (89.9, 53.6 and 97.3 mV dec^{-1}), further indicating that the redox conversion of CoNCNF was fast.

3.4. Electrochemical properties of the CoNCNF modified Li-S battery

The cells with the CoNCNF interlayers were assembled to systematically evaluate electrochemical performance. A series of constant current charge-discharge tests were carried out. The cyclic stability of the cells at a current of 1 C is shown in Fig. 5a. The CoNCNF-based cell had an excellent initial capacity of 1023.9 mAh g^{-1} and remained at 746.2 mAh g^{-1} after 1000 cycles. However, the cell with the NCNF interlayers had an initial capacity of 1001.3 mAh g^{-1} and the capacity rapidly decreased to 302.2 mAh g^{-1} after 700 cycles. Worst of all was the bare S cell, which provided an initial capacity of only 786 mAh g^{-1}, fading rapidly to 647.6 mAh g^{-1} after 90 cycles. The high capacity reflects that the catalytic effect of CoNCNF enhances the reaction limit and S utilization. Combining the charge-discharge curves makes it easier to analyze the catalytic mechanism, as shown in Fig. 5b, the three types of cells show a typical one charging plateau and two discharging plateaus. The cell with the CoNCNF interlayer shows a lower charging potential and a higher discharging potential than those of the contrast sample. The smaller potential difference ΔE (Fig. 5b) indicates that the implantation of single-atom Co enhances the catalytic activity of the S redox reaction decreasing the electrochemical polarization. In addition, the smaller ΔE of the CoNCNF cell is also reflected in the different stages of the whole cycle (Fig. S10). Fig. S11 clearly shows that the CoNCNF has a higher reduction potential and lower oxidation potential at the onset of discharging-charging, demonstrating that the single-atom Co has significantly lowered the reaction energy barrier of S and Li$_2$S onset in the solid phase. The first discharge plateau at ~2.3 V is ascribed to the reduction of S$_8$ to Li$_2$S$_4$, while the second discharge plateau at ~2.1 V originates from the reduction of Li$_2$S$_4$ to Li$_2$S. Because the conversion of Li$_2$S$_4$ to Li$_2$S contributes 75% of capacity in the whole discharge process, more importantly, this process is a solid-solid conversion and the high reaction energy barrier seriously affects the reaction limit. Therefore, analysis of the capacity ratio (Q2/Q1) of the second to the first discharge
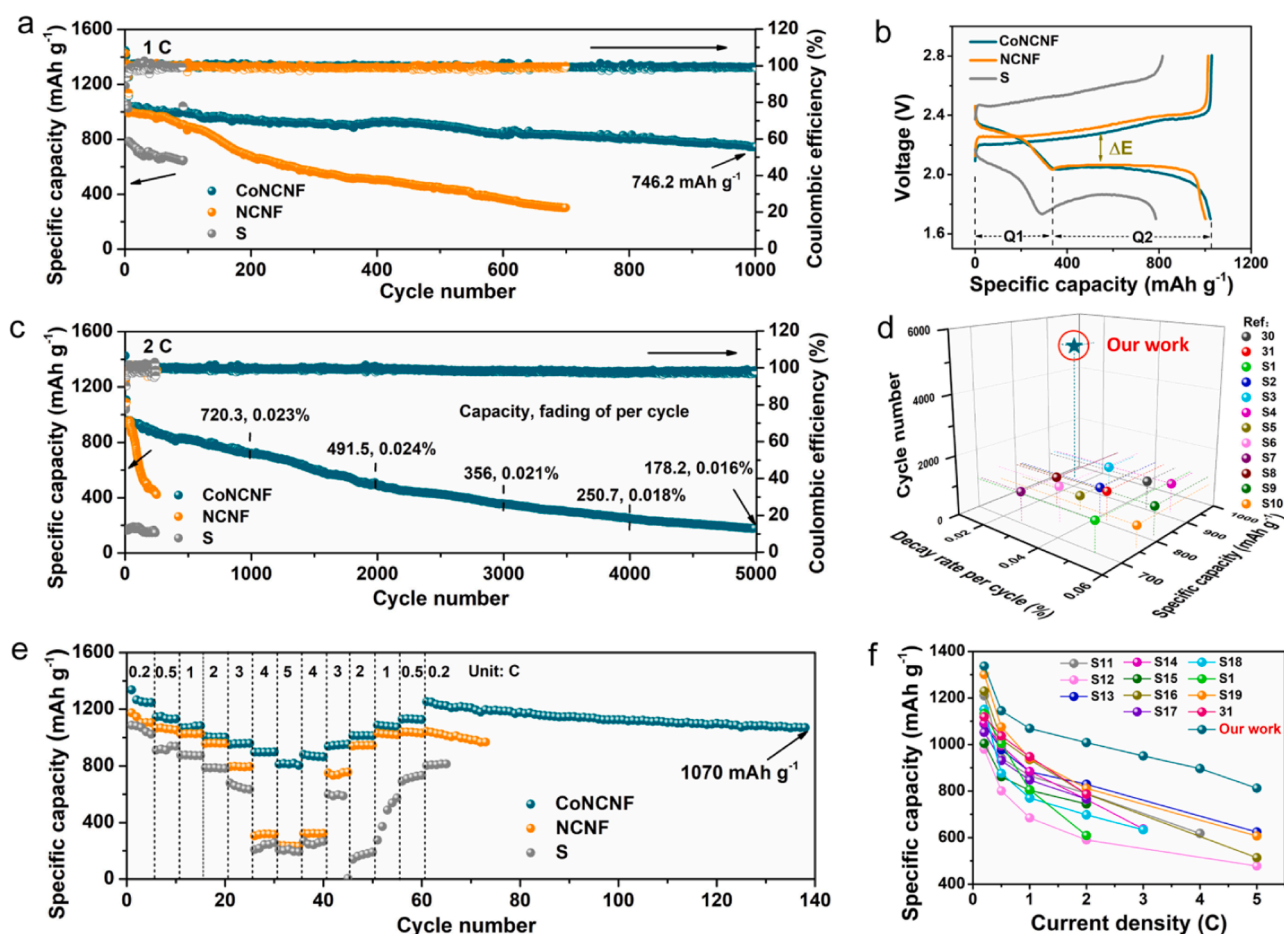

Fig. 5. (a) Long-term cycling performance and (b) initial charge-discharge capacity-voltage curve at 1 C. (c) Long-term cycling performance and (d) compared with similar work at 2 C. (e) Rate performance and (f) comparison of similar work.

plateau is an important reference to study kinetics of the discharge process. Obviously, the higher Q2/Q1 of CoNCNF cell proves that it promotes the catalysis between solids-solids. In addition, polysulfide penetration experiments of the separator were carried out using H-cell (Fig. S12). The CoNCNF interlayer can effectively inhibit the polysulfide shuttle, obviously superior to the NCNF interlayer, while serious polysulfide shuttle could be observed for the pure PP separator. To further indicate the inhibition of shuttle effect by the CoNCNF interlayer, the cell after 250 cycles was disassembled and the surface morphology of the Li anode was observed. The disassembled photos clearly show that the pure PP separator is yellow, and the separator with the NCNF interlayer is light yellow (Fig. S13). Hardly yellow color could be observed for the corresponding separator with the CoNCNF interlayer, presenting that the polysulfide shuttle has been effectively inhibited. SEM images of the Li anode after cycling (Fig. S14) show the dense and smooth surface of the Li anode protected with CoNCNF interlayer, indicating less corrosion by polysulfides. The surface of Li anode corresponding to the NCNF intermediate layer is rough. The surface of the Li anode related to the pure PP separator is critically rough with large particles aggregated, indicating more serious corrosion by polysulfides. In addition, the EDS mapping shows that the Li anode surface of the CoNCNF interlayer has a lower content of sulfur than that of the other two cells, indicating that the CoNCNF interlayer provides effective inhibition for the polysulfide shuttle. Further increasing the discharge current to 2 C, the CoNCNF interlayer cell still maintained a high discharge capacity of 936.2 mAh g^{-1} (Fig. 5c). More surprisingly, it cycled 5000 cycles at an extremely low fading rate of 0.016% per cycle and the final capacity of 178.2 mAh g^{-1} was parallel to that of some fresh cathode material such as LiFePO$_4$. It fully demonstrates that the cell with CoNCNF catalyst has high S utilization and excellent cyclic stability due to sustainable activity of the catalyst. It is because of efficient suppression of the polysulfides shuttle effect that excellent long-cycle stability of the cell is maintained. We compare the main parameters such as cycle number, decay rate par cycle and discharge specific capacity at 2 C with the state-of-the art reports and count them in Fig. 5d and Table S2. It is clear that our work has a greater advantage. Similarly, the kinetic conversion of CoNCNF accelerated LiPSs is also reflected in the rate performance of the cell. At the cycling rates of 0.2, 0.5, 1, 2, 3 and 4 C, the CoNCNF cell achieved discharge capacities of 1336.9, 1144.7, 1069.2, 1008.6, 951.0 and 896.5 mAh g^{-1} (Fig. 5e), respectively, and surprisingly, it still contributed a discharge capacity of 812.6 mAh g^{-1} even at the ultra-high rate of 5 C, which is almost four times the discharge capacity of the contrast sample. The charge-discharge capacity-voltage curve of the CoNCNF cell showed a much flatter plateau (Fig. S15). The second discharge plateau disappeared at only 4 C for NCNF cell due to the huge polarization (Fig. S15). The excellent rate performance is attributed to the high catalytic activity and the cross-linked hollow fiber structure of the interlayer. On the one hand, it catalyzes the effective conversion of LiPSs to enhance the utilization of active substances, and on the other hand, the cross-linked hollow fibers and gaps are conducive to rapid electron/ion transports. This is further demonstrated by the diffusion rate of Li ions. Fig. S16 records the CV tests at different sweep rates. Three typical redox peaks appeared for each cell. It is clear that the CoNCNF cell had the highest peak and the smallest shift with increasing sweep rate. Also, the calculated Li ions diffusion rate for each peak corresponding to the CoNCNF cell was the highest. In addition, it can be seen from the Nyquist plot (Fig. S17) that the CoNCNF had the smallest charges transfer impedance and the highest ions diffusion rate, which are consistent with the above analyses. The initial capacity of the CoNCNF cell still reached a high capacity of 1252.7 mAh g^{-1} at 0.2 C after 60 cycles at different current densities, and remained at 1070.3 mAh g^{-1} after 140 cycles. This work has a huge advantage in terms of high rate compared to previous similar reports (Fig. 5f and Table S3). The rate performance further demonstrates that the CoNCNF has excellent catalytic ability enabling the discharge capacity to be improved.

To demonstrate the capability of CoNCNF in practical applications,

we further increased the S mass loading to 12.5 mg cm^{-2} in cathode (Fig. 6a), it was still able to provide a high capacity of 10.7 mAh cm^{-2} at 0.1 C, which remained at 7.7 mAh cm^{-2} after 150 cycles, nearly twice that of the commercial Li-ion batteries. The corresponding charge-discharge curves showed a clear and complete plateau (Fig. 6b). The electrochemical performance of the high mass loading has a significant advantage over similar previous reports (Fig. 6c and Table S4). Pouch cells with the sulfur loading of 5 mg cm^{-2} and the E/S ratio of 8 μL mg^{-1} were assembled to identify the performance of CoNCNF interlayer for practical application. An open-circuit voltage of 2.8 V was achieved for the assembled pouch cells. A high initial specific capacity of 1071.4 mAh g^{-1} was obtained and a good capacity of 882.7 mAh g^{-1} maintained after 39 cycles at a current density of 0.1 C (Fig. S18), indicating the well application ability of the CoNCNF interlayer.

To further investigate the catalytic mechanism, theoretical calculations of Gibbs free energy were performed. The optimized structures of the intermediates and their Gibbs free energy distribution are shown in Fig. 6d, and it is not difficult to find that after the spontaneous exothermic transformation from S$_8$ to Li$_2$S$_8$, the subsequent four steps of forming Li$_2$S$_6$, Li$_2$S$_4$, Li$_2$S$_2$ and Li$_2$S are all heat-absorbing steps. Among them, the formation of Li$_2$S from Li$_2$S$_2$ has the largest positive Gibbs free energy, which indicates that it is the rate limiting step in the whole discharge process. We have calculated that the free energy of this step for CoNCNF is significantly smaller than that of the NCNF sample, indicating that the implanted single-atom Co can reduce the reduction energy barrier of Li$_2$S$_2$ and promote its catalytic conversion. The catalytic process can be more easily understood by Fig. 6e, f. The implantation of single-atom Co makes it easier for electrons to jump and lowers reaction energy barrier for the LiPSs conversion. The hollow carbon nanoreactors integrate 1D fibrous structure interconnected to achieve rapid ion/electron transports. The synergy of the two achieves a significant increase in the electrocatalysis.

4. Conclusion

In summary, a novel CoNCNF with single-atom Co implanted in 1D free-standing cross-linked hollow carbonaceous nanovesicles has been successfully prepared and used in the cathode-separator interlayer of modified Li-S batteries. The unique atomically distributed CoN$_4$ sites of CoNCNF increase the large binding energy to LiPSs and lower the reaction energy barrier, which effectively limit the shuttle effect. The cross-linked hollow carbon nanovesicles are profitable for storage of electrolytes facilitating ions transport and their excellent conductive walls of the well contacted holes are more conducive to the fast transmission of electrons. The efficient and stable catalytic performance of CoNCNF enables the Li-S battery not only to provide a high capacity of 812.6 mAh g^{-1} at the high current density of 5 C but also to operate at a very low fading rate (0.016%) of 5000 cycles at 2 C. In addition, it still ensures a high areal capacity of 10.7 mAh cm^{-2} for the Li-S battery when the cathode S mass loading is 12.5 mg cm^{-2}. Thus, our work opens up a new direction for the commercialization of high-performance Li-S batteries based on restraining shuttle effect by effective adsorption and electrocatalysis for LiPSs over the advanced single-atom catalysts in hollow carbonaceous nanovesicle fibers.

CRediT authorship contribution statement

Huifeng Zhuang: Conceptualization, Formal analysis, Methodology, Writing – original draft. **Tengfei Zhang:** Formal analysis. **Hong Xiao:** Formal analysis. **Fanchao Zhang:** Formal analysis. **Pinyu Han:** Formal analysis. **Hongfei Gu:** Formal analysis. **Junrong Jiao:** Formal analysis, Methodology. **Wenxing Chen:** Formal analysis, Methodology. **Qiuming Gao:** Conceptualization, Formal analysis, Methodology, Writing – review & editing, Supervision, Funding acquisition.
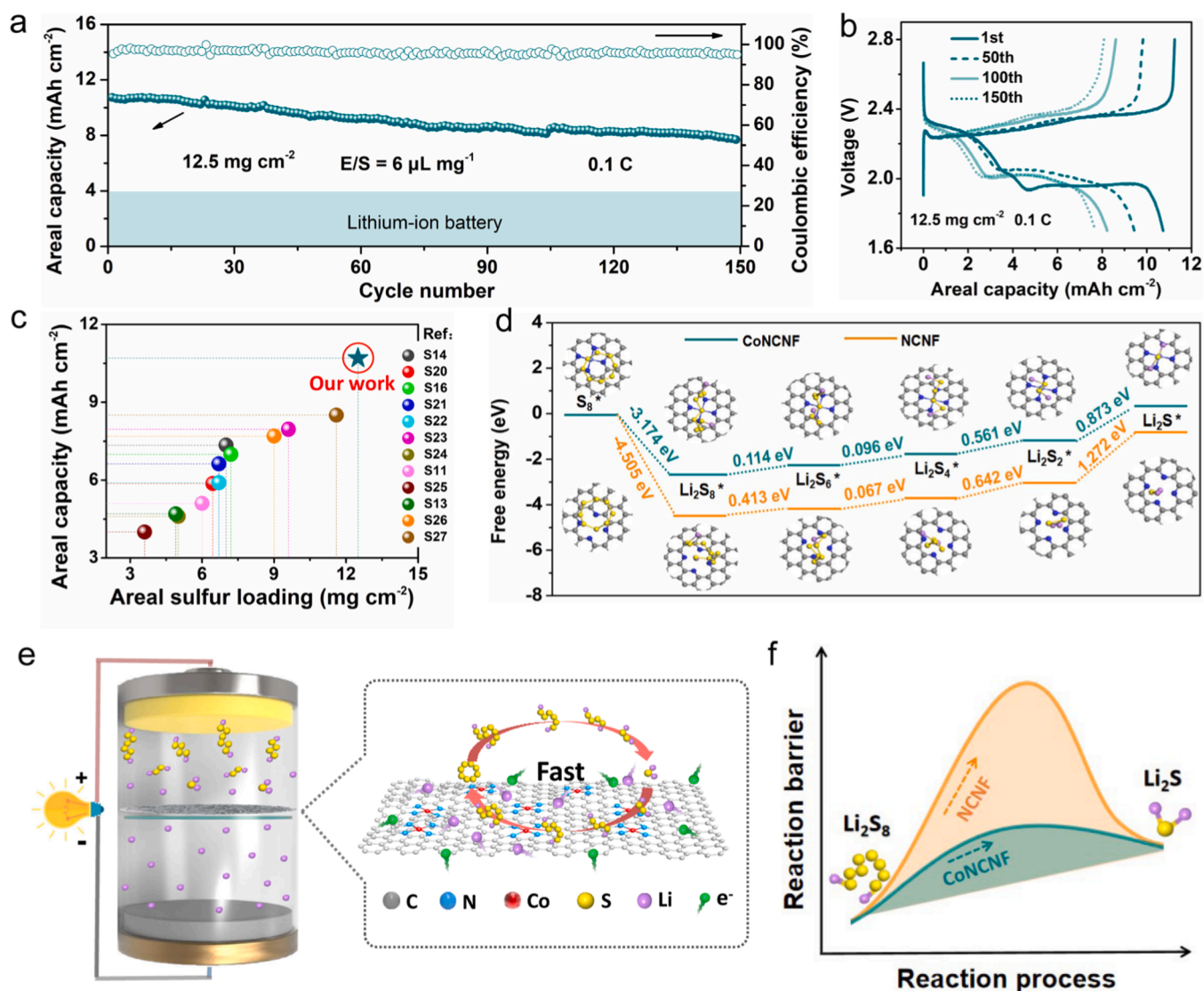
Fig. 6. (a) Long-term cycling performance of CoNCNF with high-sulfur mass loading and (b) different stages of charge-discharge capacity-voltage curves at 0.1 C. (c) Comparison of similar work. d) Energy profiles for the reduction of LiPSs on CoNCNF and NCNF substrates. Insets are the optimized adsorption conformations. (e) The schematic catalytic reactions over the CoNCNF. And (f) schematic diagram of the catalytic reactions on CoNCNF and reducing the LiPSs reduction barrier.

Declaration of Competing Interest

The authors declare that they have no known competing financial interests or personal relationships that could have appeared to influence the work reported in this paper.

Data availability

Data will be made available on request.

Acknowledgments

Appendix A. Supporting information

Supplementary data associated with this article can be found in the online version at doi:10.1016/j.apcatb.2023.123273.

References

[1] P.G. Bruce, S.A. Freunberger, L.J. Hardwick, J.-M. Tarascon, Li-O$_2$ and Li-S batteries with high energy storage, Nat. Mater. 11 (2012) 19.
[2] L. Konga, Q. Jin, X. Zhang, B. L, J. Chen, W. Zhu, J. Huang, Q. Zhang, Towards full demonstration of high areal loading sulfur cathode in lithium-sulfur batteries, J. Energy Chem. 39 (2019) 17.
[3] W. Guo, W. Zhang, Y. Si, D. Wang, Y. Fu, A. Manthiram, Artificial dual solid-electrolyte interfaces based on in situ organothiol transformation in lithium sulfur battery, Nat. Commun. 12 (2021) 3031.
[4] X. Hong, J. Mei, L. Wen, Y. Tong, A.J. Vasileff, L. Wang, J. Liang, Z. Sun, S.X. Dou, Nonlithium metal-sulfur batteries: steps toward a leap, Adv. Mater. 31 (2019), 1802822.
[5] J. Balach, H.K. Singh, S. Gomoll, T. Jaumann, M. Klose, Synergistically enhanced polysulfide chemisorption using a flexible hybrid separator with N and S dual-doped mesoporous carbon coating for advanced lithium-sulfur batteries, ACS Appl. Mater. Interfaces 8 (2016) 14586–14595.
[6] P. Wang, Z. Zhang, X. Yan, M. Xu, Y. Chen, J. Li, J. Li, K. Zhang, Y. Lai, Pomegranate-like microclusters organized by ultrafine Co nanoparticles@nitrogen-doped carbon subunits as sulfur hosts for long-life lithium-sulfur batteries, J. Mater. Chem. A 6 (2018) 14178.

[7] J. Qian, Y. Xing, Y. Yang, Y. Li, K. Yu, W. Li, T. Zhao, Y. Ye, L. Li, F. Wu, R. Chen, Enhanced electrochemical kinetics with highly dispersed conductive and electrocatalytic mediators for lithium-sulfur batteries, Adv. Mater. 33 (2021), 2100810.

[8] R. Chen, T. Zhao, F. Wu, From a historic review to horizons beyond: lithium-sulphur batteries run on the wheels, Chem. Commun. 51 (2015) 18.

[9] G. Li, J. Sun, W. Hou, S. Jiang, Y. Huang, J. Geng, Three-dimensional porous carbon composites containing high sulfur nanoparticle content for high-performance lithium-sulfur batteries, Nat. Commun. 7 (2016) 10601.

[10] Y. Yang, G. Zheng, Y. Cui, Chem, Nanostructured sulfur cathodes, Soc. Rev. 42 (2013) 3018.

[11] X. Liang, Y. Rangom, C.Y. Kwok, Q. Pang, L.F. Nazar, Interwoven MXene nanosheet/carbon-nanotube composites as Li-S cathode hosts, Adv. Mater. 29 (2017), 1603040.

[12] S.H. Chung, A. Manthiram, Rational design of statically and dynamically stable lithium-sulfur batteries with high sulfur loading and low electrolyte/sulfur ratio, Adv. Mater. 30 (2018), 1705951.

[13] H.L. Pan, J.Z. Chen, R.G. Cao, V. Murugesan, N.N. Rajput, K.S. Han, K. Persson, L. Estevez, M.H. Engelhard, J.G. Zhang, K.T. Mueller, Y. Cui, Y.Y. Shao, J. Liu, Non-encapsulation approach for high-performance Li-S batteries through controlled nucleation and growth, Nat. Energy 2 (2017) 813.

[14] J. Wang, G. Li, D. Luo, Y. Zhang, Y. Zhao, G. Zhou, L. Shui, X. Wang, Z. Chen, Engineering the conductive network of metal oxide-based sulfur cathode toward efficient and longevous lithium-sulfur batteries, Adv. Energy Mater. 84 (2020), 105891.

[15] H. Yang, Y. Wu, G. Li, Q. Lin, Q. Hu, Q. Zhang, J. Liu, C. He, Scalable production of efficient single-atom copper decorated carbon membranes for CO_2 electroreduction to methanol, J. Am. Chem. Soc. 141 (2019) 12717–12723.

[16] R. Zhang, X. Chen, X. Shen, X.-Q. Zhang, Xi-R. Chen, X.-B. Cheng, C. Yan, C.-Z. Zhao, Q. Zhang, Coralloid carbon fiber-based composite lithium anode for robust lithium metal batteries, Joule 2 (2018) 1–14.

[17] H. Zhuang, T. Zhang, H. Xiao, X. Liang, F. Zhang, J. Deng, Q. Gao, 3D free-standing carbon nanofibers modified by lithiophilic metals enabling dendrite-free anodes for Li metal batteries, Energy Environ. Mater. 6 (2023), e12470.

[18] D. Wang, F. Li, M. Liu, G. Lu, H. Cheng, 3D aperiodic hierarchical porous graphitic carbon material for high-rate electrochemical capacitive energy storage, Angew. Chem. Int. Ed. 47 (2008) 373–376.

[19] Y. Liu, Z. Ma, G. Yang, Z. Wu, Y. Li, J. Gu, J. Gautam, X. Gong, A. Chishti, S. Duan, C. Chen, M. Chen, L. Ni, G. Diao, Multifunctional $ZnCo_2O_4$ quantum dots encapsulated in carbon carrier for anchoring/catalyzing polysulfides and self-repairing lithium metal anode in lithium-sulfur batteries, Adv. Funct. Mater. 32 (2022) 2109462.

[20] Y. Song, W. Cai, L. Kong, J. Cai, Q. Zhang, J. Sun, Rationalizing electrocatalysis of Li-S chemistry by mediator design: progress and prospects, Adv. Energy Mater. 10 (2020), 1901075.

[21] Y. Zhang, J. Liu, J. Wang, Y. Zhao, D. Luo, A. Yu, X. Wang, Z. Chen, Engineering oversaturated Fe-N_5 multifunctional catalytic sites for durable lithium-sulfur batteries, Angew. Chem. Int. Ed. 60 (2021) 26622.

[22] Q. Zhang, Q. Huang, S.-M. Hao, S. Deng, Q. He, Z. Lin, Y. Yang, Polymers in lithium-sulfur batteries, Adv. Sci. 9 (2022), 2103798.

[23] Z.W. Seh, Y. Sun, Q. Zhang, Y. Cui, Designing high-energy lithium-sulfur batteries, Chem. Soc. Rev. 45 (2016) 5605–5634.

[24] L. Wang, Z.-Y. Wang, J.-F. Wu, G.-R. Li, S. Liu, X.-P. Gao, To effectively drive the conversion of sulfur with electroactive niobium tungsten oxide microspheres for lithium-sulfur battery, Nano Energy 77 (2020), 105173.

[25] D.R. Deng, F. Xue, Y.J. Jia, J.C. Ye, C.D. Bai, M.S. Zheng, Q.F. Dong, Co_4N nanosheet assembled mesoporous sphere as a matrix for ultrahigh sulfur content lithium-sulfur batteries, ACS Nano 11 (2017) 6031.

[26] W. Yao, W. Zheng, J. Xu, C. Tian, K. Han, W. Sun, S. Xiao, ZnS-SnS@NC heterostructure as robust lithiophilicity and sulfiphilicity mediator toward high-rate and long-life lithium-sulfur batteries, ACS Nano 15 (2021) 7114–7713.

[27] J. Wang, Li, T. Zhang, Heterogeneous single-atom catalysis, Nat. Rev. Chem. 2 (2018) 65–81.

[28] X. Liang, Z. Li, H. Xiao, T. Zhang, P. Xu, H. Zhang, Q. Gao, L. Zheng, Two types of single-atom FeN_4 and FeN_5 electrocatalytic active centers on N-doped carbon driving high performance of the SA-Fe-NC oxygen reduction reaction catalyst, Chem. Mater. 33 (2021) 5542–5544.

[29] Y. Zhang, C. Kang, W. Zhao, Y.J. Song, J.M. Zhu, H. Huo, Y.L. Ma, C.Y. Du, P. J. Zuo, S.F. Lou, G.P. Yin, d-p Hybridization-induced "trapping-coupling-conversion" enables high-efficiency Nb single-atom catalysis for Li-S batteries, J. Am. Chem. Soc. 145 (2023) 1728–1739.

[30] F. Zhang, Z. Tang, T. Zhang, H. Xiao, H. Zhuang, X. Liang, L. Zheng, Q. Gao, Atomically distributed asymmetrical five-coordinated Co-N_5 moieties on N-rich doped C enabling enhanced redox kinetics for advanced Li-S batteries, J. Mater. Chem. A 10 (2022) 22114–22124.

[31] T. Zhang, H. Xiao, X. Liang, F. Zhang, H. Zhuang, Q. Gao, L. Zheng, Dual-atom nickel moieties of Ni(II)$_2$N4(μ_2-N)$_2$ anchored on alfalfa-derived developed porous N-doped carbon for high-performance Li-S battery, Small 18 (2022) 2201996.

[32] H. Yang, Q. Lin, C. Zhang, X. Yu, Z. Cheng, G. Li, Q. Hu, X. Ren, Q. Zhang, J. Liu, C. He, Carbon dioxide electroreduction on single-atom nickel decorated carbon membranes with industry compatible current densities, Nat. Commun. 11 (2020) 593.

[33] H. Yang, Q. Lin, Y. Wu, G. Li, Q. Hu, X. Chai, X. Ren, Q. Zhang, J. Liu, C. He, Highly efficient utilization of single atoms via constructing 3D and free-standing electrodes for CO_2 reduction with ultrahigh current density, Nano Energy 70 (2020), 104454.

[34] Y.J. Si, C.G. Chen, W. Yin, H. Cai, The synthesis and characterization of a Co-N/C composite catalyst for the oxygen reduction reaction in acidic solution, Chin. Sci. Bull. 56 (2011) 1086–1091.

[35] Y. Min, X. Zhou, J.-J. Chen, W. Chen, F. Zhou, Z. Wang, J. Yang, C. Xiong, Y. Wang, F. Li, H.-Q. Yu, Y. Wu, Integrating single-cobalt-site and electric field of boron nitride in dechlorination electrocatalysts by bioinspired design, Nat. Commun. 12 (2021) 303.

[36] Y.Q. Zhu, W.M. Sun, W.X. Chen, T. Cao, Y. Xiong, J. Luo, J.C. Dong, L.R. Zheng, J. Zhang, X.L. Wang, C. Chen, Q. Peng, D.S. Wang, Y.D. Li, Scale-up biomass pathway to cobalt single-site catalysts anchored on N-doped porous carbon nanobelt with ultrahigh surface area, Adv. Funct. Mater. 28 (2018), 1802167.

[37] Y.H. Han, Y.G. Wang, W.X. Chen, R.R. Xu, L.R. Zheng, J. Zhang, J. Luo, R.A. Shen, Y.Q. Zhu, W.C. Cheong, C. Chen, Q. Peng, D.S. Wang, Y.D. Li, Hollow N-doped carbon spheres with isolated cobalt single atomic sites: superior electrocatalysts for oxygen reduction, J. Am. Chem. Soc. 139 (2017) 17269–17272.

[38] Y.H. Han, Z.Y. Wang, R.R. Xu, W. Zhang, W.X. Chen, L.R. Zheng, J. Zhang, J. Luo, K.L. Wu, Y.Q. Zhu, C. Chen, Q. Peng, D. Liu, P. Hu, D.S. Wang, Y.D. Li, Ordered porous nitrogen-doped carbon matrix with atomically dispersed cobalt sites as an efficient catalyst for dehydrogenation and transfer hydrogenation of N-heterocycles, Angew. Chem. Int. Ed. 57 (2018) 11262–11266.

[39] Z. Shen, X. Jin, J. Tian, M. Li, Y. Yuan, S. Zhang, S. Fang, X. Fan, W. Xu, H. Lu, J. Lu, H. Zhang, Cation-doped ZnS catalysts for polysulfide conversion in lithium-sulfur batteries, Nat. Catal. 5 (2022) 555–563.